Research Article | Vol. 40, No. 6 / June 2023 / Journal of the Optical Society of America A | 1191

Journal of the Optical Society of America A
OPTICS, IMAGE SCIENCE, AND VISION

Star map matching method for optical circular rotation imaging based on graph neural networks

Tingting Xu,[1,2,3] Xiubin Yang,[1,2,*] Zongqiang Fu,[1,2] Ge Jin,[3,4] Wei Chen,[5,6] Miaoran Huang,[7] and Guoyu Lu[3]

[1] Changchun Institute of Optics, Fine Mechanics and Physics, Chinese Academy of Sciences, Changchun 130033, China
[2] University of Chinese Academy of Sciences, Beijing 100049, China
[3] School of Electrical and Computer Engineering, College of Engineering, University of Georgia, Athens, Georgia 30602, USA
[4] School of Mechanical and Power Engineering, Nanjing Tech University, Nanjing 21186, China
[5] School of Computer Science & Technology, China University of Mining and Technology, Xuzhou, 221116, China
[6] School of Mechanical Electronic & Information Engineering, China University of Mining and Technology-Beijing, Beijing, 100083, China
[7] Wu Yuzhang Honors College, Sichuan University, Chengdu 610065, China
*yangxiubin@ciomp.ac.cn

Received 26 January 2023; revised 8 April 2023; accepted 3 May 2023; posted 4 May 2023; published 30 May 2023

This paper focuses on a dynamic star image acquisition and matching method for space situational awareness, which can quickly search for widely distributed resident space objects. First, the optical circular rotation imaging method performed by a single space camera is proposed to obtain a series of star images. And then, the image matching method based on graph neural networks is proposed for generating a wide observation star image. Experiment results show that compared with baseline matching algorithms, the matching accuracy and matching precision of the proposed algorithm are improved significantly.

https://doi.org/10.1364/JOSAA.486401

1. INTRODUCTION

With the rapid increase in the number of resident space objects (RSOs) that include spacecraft, spent rocket bodies, and other catalogued debris, the potential of collision between RSOs and space assets increases quickly [1]. Space situational awareness (SSA) plays a pivotal role in preventing collisions by surveilling the movement of the space objects [2]. Compared with ground-based telescopes, space-based detectors are more feasible to observe RSOs because of their advantages in eliminating weather conditions and observation station locations [3,4]. The wide distribution of RSOs in space and the limited field of view (FOV) of optical payloads are two significant constrains in SSA [5].

Space-based observations often stitch images from multiple cameras to expand the observation area, which results in low imaging efficiency and high cost [6–9]. Therefore, researchers propose dynamic imaging modes to overcome shortages of multiple-camera systems. The European Space Agency proposed a Gaia mission to produce the largest and most precise three-dimensional space map of our galaxy [10]. The measurement principle of Gaia is scanning space astrometry, which relies on a slowly scanning satellite equipped with two CCD telescopes to obtain the absolute parallaxes. And the scanning of the Gaia satellite should cover as much sky space as possible in a short time. The Harbin Institute of Technology proposed a novel optical scanning imaging mode to extend the ground coverage in remote sensing [11]. This mode employs one inclined space camera that rotates around the nadir axis based on the high agility of satellites to achieve wide-swath imaging. Inspired by these two kinds of imaging modes, we proposed the optical circular rotation imaging (SOCRI) method to search widely distributed RSOs. The method through one camera rotates at a constant speed around the spin axis whose direction is from the satellite to the geocentric. Because the RSOs for SSA are mainly distributed on low Earth orbit, the observation satellite is set to the low Earth orbit, and the camera is fixed on the satellite. Different from observations in remote sensing staring at the Earth surface, the optical axis of the camera in SOCRI will be pointing outwards to cover RSOs in the whole sky [12].

After star images are obtained, the image matching method for star maps is important for achieving a stitched star image with a large FOV. According to the theory of star imaging in dynamic status, the limited energy of star points is spread over several pixels on the star map, resulting in a lack of local and texture features. Therefore, the natural image matching and stitching algorithm cannot construct stable and discriminative matching features for star images. Recently, graph neural networks (GNNs) have been extensively studied for their significant performance in extracting node and graph features for topological graph [13–17]. Sarlin proposed a neural network SuperGlue (SG) through a GNN with self-(intra-image) and cross-(inter-image) attention to jointly find the best matching points between two sets of pre-existing local features [18].

Generally, the pipeline for applying the GNN to imaging matching tasks is as follows. First, the topology graph is built to transfer image information from pixel-wise to semantic. Then the stable descriptors of key points are used in the matching algorithm, and corresponding matched points are obtained to realize precise matching [19].

The star image has its own characteristics, such as bright star points, which can be directly considered as feature points in the matching method instead of corner or inflection feature points used in natural images [20,21]. In addition, there is a strong topology position relationship among star points. Each star point could be considered as a graph node to construct the unique and optimal typology graph [22]. However, the attention mechanism used in SuperGlue is a global attention mechanism, and each key point detected in the pair of images will be calculated, which brings a large amount of computation. Meanwhile, the key points detected in natural images are irrelevant, which reduces the ability of graph neural networks. Therefore, a modified SuperGlue (MSG) network is proposed to deal with the matching problem of the star image in this paper. Instead of the global attention mechanism used in SuperGlue, we adopted the graph attention networks (GAT) with mask graph attention mechanism to perform the node embedding [23]. GAT is a kind of classical GNN, which enables specifying different weights to different nodes in a neighborhood. Compared with the graph convolutional networks (GCN) [24], another classical GNN, GAT does not require any kind of costly matrix operation (such as inversion) or depend on the graph structure upfront.

The rest of the paper is organized as follows: in Section 2, the mathematical formulations of SOCRI and the imaging principle of stars on the focal plane under dynamic conditions are described. And then, the MSG model architecture, feature extraction, topology star graphs building, and the multiplex graph node embedding are explained in detail. In Section 3, the experiments are performed to validate the MSG method, and the results are analyzed. In Section 4, the conclusion and future works of this paper are given.

2. METHODS

A. Principle of the SOCRI Method

Traditional imaging modes in SSA missions limit the performance of satellites on orbit, which makes it difficult to search for widely distributed space targets quickly and efficiently. Under the conditions of limited satellite resources, the proposed SOCRI method has its advantage of low cost, unlimited FOV, and flexible attitude over these imaging modes. Benefiting from the attitude changing ability of agile satellites, the single camera could move along with the satellite and rotates around the spin axis at the same time. We considered the direction from the center of the observation satellite to the center of the Earth as the spin axis, and the spin axis will change slowly with the moving of the satellite. Therefore, the SOCRI method scans two dimensions of the space, as shown in Fig. 1. One dimension of the space is scanned by the camera that rotates with a constant velocity around the spin axis, as shown by the red circle stripe in Fig. 1. Another scanning dimension of the space is achieved by adjusting the spin axis; the camera will scan the blue circle stripe

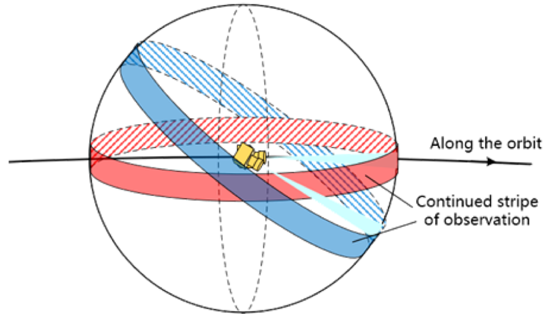

Fig. 1. Illustration diagram of the SOCRI mode. The red stripe is generated by the rotation motion of the camera rotating around the spin axis, and the blue stripe is generated through the motion of the spin axis.

as shown in Fig. 1. The method expands the coverage area and achieves the uniformity coverage of the sky area.

1. Parameters Design of SOCRI

The SOCRI mode composes of a circular rotation motion around the spin axis and an orbital motion around the orbit, and it is challenging to analyze the whole imaging process of SOCRI to design parameters. The imaging area is changing with the rotation velocity and the espouse time of the camera. To cover the most area of space, the circular rotation motion is discussed at first, as shown in Fig. 2(a), where P_i and P_j represent the image captured by the camera at times T_i and T_j, respectively. And then, the series of star images will be matched and stitched to generate a large FOV star imaging containing stars and space targets. The position relationship between two adjacent frames of star images is shown in Fig. 2(b). During the period of satellite rotation motion, the trajectory of the intersection of the optical axis of the camera and the center of the image plane is a spiral line not a circle. And the included angle θ between the first frame P_1 and the last frame P_{last} of this series images can be expressed as

$$\theta = \overline{\omega_o} \cdot T_{\text{loop}} = (1 - \beta) \cdot \alpha, \quad \textbf{(1)}$$

$$\overline{\omega_o} = \frac{1}{T_{\text{orbit}}} \int_0^{T_{\text{orbit}}} |\omega_o(t)| \mathrm{d}t, \quad \textbf{(2)}$$

where α is the camera FOV along the orbit, β is the overlap ratio between P_1 and P_{last}, and T_{loop} is the total time of the satellite to rotate one loop. Due to the influence of the perturbation force from the Earth and other planets on the satellite in orbit, the satellite angular velocity along the track ω_o is a variable value. Therefore, to simplify the derivation of the satellite rotation velocity, the mean value $\overline{\omega_o}$ is adopted. It is approximately calculated by

$$T_{\text{loop}} = \frac{(1 - \beta) \cdot \alpha}{\overline{\omega_o}}. \quad \textbf{(3)}$$

The overlap area should be considered for achieving leakless sky coverage. And then the rotation angular velocity of the camera ω_s can be calculated as follows, where η is the overlap ratio of two adjacent frames:

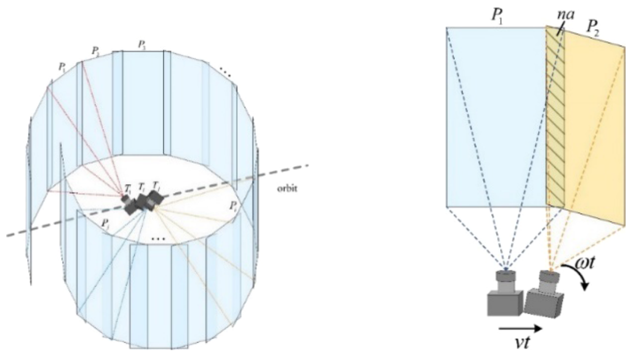

(a) (b)

Fig. 2. Processing of the SOCRI mode. (a) The change of the focal plane during the whole circle motion; (b) the position relationship of two continuous frames.

$$\omega_s = \frac{(1+\eta)\cdot 2\pi}{T_{\text{loop}}}. \tag{4}$$

2. *Imaging Principle of Star Points on the Focal Plane under Dynamic Conditions*

In order to realize the stitching of star images output from the SOCRI method, the imaging principle of star points on the focal plane under dynamic status is analyzed first [25]. When the camera is relatively stationary with the stars, the distribution of star points represents as a point on the image plane. When the camera moves relative to the stars, there will be a streak track during the exposure time. The energy distribution can be described by a two-dimensional Gaussian function $f(x, y)$ as

$$f(x, y) = A \cdot \exp\left\{-\frac{(x-x_i)^2}{2\sigma_x^2} - \frac{(y-y_i)^2}{2\sigma_y^2}\right\}, \tag{5}$$

where x_i, y_i are center positions of the star point that project to the image plane, A represents the total number of photoelectrons transformed from light energy of the stars by sensors, which affects the brightness of the star image. σ_x, σ_y are the Gaussian radius which represent the energy concentration from x, y directions, respectively.

When the camera moves relative to the stars, the positions of star points on the image plane (x_i, y_i) in Eq. (5) will change within the exposure time. According to the relationship between the camera body coordinate system and the focal plane, which is shown in Fig. 3, the direction vector of star i in the camera body coordinate system w_i can be expressed as

$$w_i = \frac{1}{\sqrt{(x_i-x_0)^2 + (y_i-y_0)^2 + f^2}} \begin{bmatrix} -(x_i-x_0) \\ -(y_i-y_0) \\ f \end{bmatrix}, \tag{6}$$

where f represents the camera focal length, and (x_0, y_0) are projection positions on the image plane of the sensor center; generally the values are (0,0) [26].

With the changing of observation satellite attitude, the positions of star points on the image plane change from $w_{i(t_0)}$ at time t_0 to $w_{i(t_0+\Delta t)}$ at time $t_0 + \Delta t$ [27], which can be expressed as

$$w_{i(t_0+\Delta t)} = M_{t_0}^{t_0+\Delta t} \times w_{i(t_0)}, \tag{7}$$

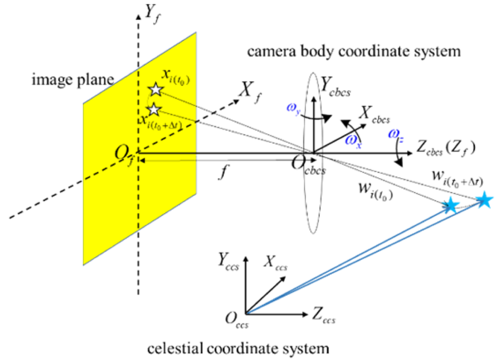

Fig. 3. Schematic diagram of the coordinate system and star points on the image in dynamic status. With camera motion, the direction vector of the star in the camera body coordinate system changes from $w_{i(t_0)}$ to $w_{i(t_0+\Delta t)}$. ω_x, ω_y, ω_z represent the components of camera velocity along three-axis.

where $M_{t_0}^{t_0+\Delta t}$ is the transformation matrix of the camera body coordinate system from time t_0 to $t_0 + \Delta t$. When Δt is closing to zero, $M_{t_0}^{t_0+\Delta t}$ can be simply expressed as

$$M_{t_0}^{t_0+\Delta t} = \begin{bmatrix} I & \omega_z \Delta t & -\omega_y \Delta t \\ -\omega_z \Delta t & I & \omega_x \Delta t \\ \omega_y \Delta t & -\omega_x \Delta t & I \end{bmatrix}, \tag{8}$$

where $I_{3\times 3}$ is the identity matrix of size 3×3, and $\omega = [\,\omega_x\ \omega_y\ \omega_z\,]^T$ represents the components of camera rotation speed along roll, pitch, and yaw directions, respectively. Combined with Eq. (6), the image positions of star i at time $t_0 + \Delta t$ can be calculated as

$$\begin{cases} x_{i(t_0+\Delta t)} = x_{i(t_0)} + y_{i(t_0)}\omega_z \Delta t + f\omega_y \Delta t \\ y_{i(t_0+\Delta t)} = y_{i(t_0)} - x_{i(t_0)}\omega_z \Delta t - f\omega_x \Delta t \end{cases}. \tag{9}$$

Therefore, combining Eq. (5) with Eq. (9), the energy distribution of stars in the image under dynamic conditions can be expressed as

$$f(x, y) = A \cdot \exp\left\{-\frac{(x-x_{i(t_0+\Delta t)})^2}{2\sigma_x^2} - \frac{(y-y_{i(t_0+\Delta t)})^2}{2\sigma_y^2}\right\}. \tag{10}$$

Since the relative motion between the camera and satellite platform is the main factor that makes star points on the image smearing, different angular velocities ω cause different dynamic states. The simulated star images under different dynamic conditions are shown in Fig. 4. Figure 4(a) is the static image because the camera is relatively stationary with the stars, and velocities along three directions are equal to zero. From Figs. 4(b)–4(d), it can be seen that ω_z is the main factor affecting the shape of the star point rather than the length of the star point. Also, the energy distribution of stars at the center is more uniform than the stars at the edge of the FOV [28]. In this work, the velocity component along the roll direction ω_z is equal to the optical axis adjusting velocity ω_o, and the velocity component ω_y is equal to the camera rotation velocity around the optical axis ω_s.

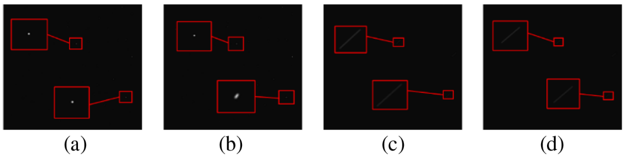

Fig. 4. Simulation star images in different angular velocity with different motion states. (a) Static image while the velocity is 0°/s; (b) only the velocity component along the roll direction; (c) only the velocity components along the pitch and yaw directions; (d) the velocity components in all directions. (a) $(\omega_x, \omega_y, \omega_z) = (0, 0, 0)$. (b) $(\omega_x, \omega_y, \omega_z) = (0, 0, 5)$. (c) $(\omega_x, \omega_y, \omega_z) = (4, 4, 0)$. (d) $(\omega_x, \omega_y, \omega_z) = (4, 4, 5)$.

B. Modified SuperGlue Network for Star Images Matching

The purpose of the proposed SOCRI method is to obtain a large FOV star image containing stars and RSOs. Therefore, the MSG network for star images matching is proposed in this section. Since the position of the star point between two adjacent frames slightly changes compared with the position of RSOs, the proposed star images matching method is implemented based on detected star points. However, star images with deep space background lack texture information and have similar star points distribution, and the traditional local features are not stable enough for star points. To overcome this shortcoming, the MSG network is proposed for constructing star point feature descriptors.

The proposed network utilizes the topological structure position information among star points to build stable descriptors from the GNN framework. The framework of the GNN is divided into two parts: message passing and message aggregation [29]. The initial features of each node pass through the message passing function to generate new features at first, and the final node features are obtained by aggregating the neighbor node messages. GCN and GAT are two classical GNNs, and the difference between message passing functions of them leads to different performance. Since GCN relies on the graph structure, a network trained on a specific graph structure cannot be directly applied to different graph structures. Therefore, GAT is selected in this paper to calculate star points features. The local graph attention mechanism is used to weight and sum the neighbor node features, which can not only reduce the cost of matrix operation, but also ensure that the learning parameters are not affected by the change of the graph structure.

1. *Model Architecture*

The proposed MSG network is built upon SuperGlue and the pipeline of MSG is shown in Fig. 5. MSG consists of four parts: initial feature descriptor encoder, graph building, graph node embedding, and graph optimal matching. In the initial feature descriptor encoder part, SuperPoint (SP) is adopted because of its pixel-wise precision, stable and fast advantage compared with the traditional handcraft feature extraction method [30]. Different from the irrelevant detected points in natural images, star points are regularly distributed in star images. Therefore, topology star graphs are built for multiplex graph node embedding, which includes self-attention for intra-graph and cross-attention for inter-graph. Then the final node

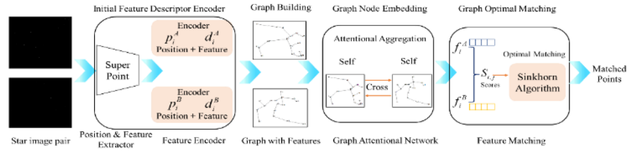

Fig. 5. Pipeline of the proposed MSG algorithm.

feature descriptors embedded with the graph structure will be solved by the optimal matching network to obtain matched points. The node embedding part of this paper is based on GAT, and the attention mechanism is mask graph attention.

2. *Building the Topology Graph Data*

Viniavskyi *et al.* proved that local features used in SuperGlue significantly affect the network performance [31]. Therefore, SuperPoint is used for extracting the position p_i, and the local features d_i for each star point. And then, p_i is embedded into a high-dimensional vector with a multilayer perceptron and combined with d_i to encode the initial representation ${}^{(0)}h_i$ for each star point [18]. Figure 6 shows the structure of the feature extracting process, and ${}^{(0)}h_i$ can be expressed as

$$ {}^{(0)}h_i = d_i + \mathrm{MLP}_{\mathrm{enc}}(p_i). \tag{11} $$

The GNN only takes graph data as the input for node embedding, and detected star points V_i should be constructed as a topology graph $G_{i(cwg)} = (V_i, E_i)$, where E_i represents the set of edges between star points. To learn more information from detected points, $G_{i(cwg)}$ is built as a fully connected weighted graph, which means each detected point in the image relates to another point, and each edge between a pair of points is weighted. Since star points are regularly distributed, the angular distance $\theta_{i,j}$ between the pair of star points $i, j\ \forall i \in V_A, \forall j \in V_A$ can be applied as the weight of the edge [32], where V_A represent the set of star points on image A. Figure 7 shows the framework of topology graph generation from star points. Therefore, the adjacency matrix $A_{i(cwg)}$ of $G_{i(cwg)}$ can be described as

$$ A_{i(cwg)}(i, j) = \theta_{i,j} = \arccos(v_i^A, v_j^A), \tag{12} $$

where v_i^A, v_j^A represent the unit direction vector of star point i, j in the camera body coordinate system, respectively.

To reduce the computational cost of the next multiplex graph node embedding module, the main spanning tree (MST) of $G_{i(mst)} = (V_i, E_{i(mst)})$ is generated by the Kruskal algorithm [33]. This MST is later considered as the input graph structure of the node embedding network. We finally pack the initial

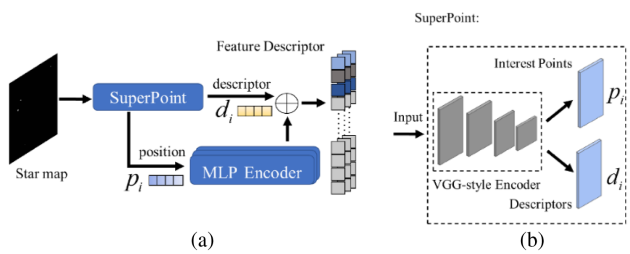

Fig. 6. Structure of the feature extracting process. (a) Feature descriptor encoder, (b) the structure of SuperPoint [31].

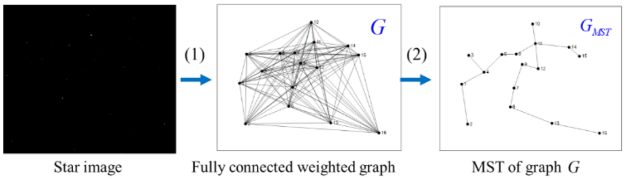

Fig. 7. Framework of topology graph generation from star points. (1) Extract star points from the processed star image. (2) Build the fully connected weighted graph $G_{i(cwg)}$ by viewing star points as nodes and viewing the angular distance between two-star points as weighted edges, where the fully connected graph means that each star point in the graph relates to another point. (3) Generate the MST $G_{i(mst)}$ of $G_{i(cwg)}$ by the Kruskal algorithm [33].

Table 1. Algorithm 1: Topology Graph Data Building

Algorithm 1: Topology Graph Data Building
Input: A pair of star images (A, B)
1. features and positions of star points extraction Eq. (11)
2. build undirected full connected weighted graphs G_A from $i, j\ \forall i \in V_A, \forall j \in V_A$ by Eq. (12)
3. generate the MST $G_{A(mst)}$, $G_{B(mst)}$ of G_A, G_B by Kruskal algorithm
Output: Topology Graph Data of star images
$G_A = \{^{(0)}h_i^A, E_{A(mst)}\}, i \in V_A, G_B = \{^{(0)}h_j^B, E_{B(mst)}\}, j \in V_B$

representation $^{(0)}h_i$ for the node from V_i with the $E_{i(mst)}$ as the initial graph data $G_i = \{^{(0)}h_i^A, E_{i(mst)}\}$. Algorithm 1 (Table 1) describes the building of topology graph data.

3. Multiplex Graph Node Embedding

In the proposed MSG network, we take a pair of graphs as input and compute the intra-graph embedding and the cross-graph embedding. For the intra-graph embedding, features are aggregated from nodes of the intra-graph. And for the cross-graph embedding, features in one graph are computed by the similar features from another graph [34,35]. Therefore, descriptors computed by the multiplex graph node embedding combine the information from image pairs and are stable for star points.

Figure 8 shows the illustration of multiplex graph node embedding. In the first step of node message propagation, the initial representation $^{(0)}h_i$ of nodes from images A and B will be separately input to the GAT for self-embedding. In the next step, intra-graph embedding features $^{(l)}h_i^A$ and $^{(l)}h_i^B$ will be jointly input for cross-embedding. Finally, the feature descriptors of star points after the multiplex graph node embedding $^{(l+1)}h_i^A, {}^{(l+1)}h_j^B$ can be expressed as

$$^{l+1}h_i^A = {}^{(l)}h_i^A + \Delta^{(l)}h_i^A, \quad ^{l+1}h_j^B = {}^{(l)}h_j^B + \Delta^{(l)}h_j^B, \tag{13}$$

where $^{(l)}h_i^A$ are the output features after performing self-attention $\alpha_{ij}^{(l)}$ on the nodes of the intra-image:

$$^{(l)}h_i = \sigma\left(\sum_{j\in N(i)} \alpha_{ij}^{(l)} W^{(l-1)} h_j\right). \tag{14}$$

And the self-attention mechanism used in GAT is masked attention, which only computes attentions from neighborhood nodes of the current node. To make attention coefficients easily comparable across different nodes, GAT normalizes them using the softmax function:

$$\alpha_{ij} = \frac{\exp(\text{Leaky ReLU}(\vec{a}^T[^{(l)}Wh_i || ^{(l)}Wh_j])}{\sum_{k\in N(i)} \exp(\text{Leaky ReLU}(\vec{a}^T[^{(l)}Wh_i || ^{(l)}Wh_k])}, \tag{15}$$

where $^{(l)}W$ is a weight matrix shared by every node in the graph. We need to perform at least one linear transformation based on the input features, and the weight matrix $^{(l)}W$ is the transform relationship between input features $^{(l-1)}h_i$ and output features $^{(l)}h_i$. In addition, $||$ is the concatenation operation, $\vec{a}$ is a weight vector to project concatenated high-dimensional features to a real number, and the LeakyReLU nonlinearity is applied.

$\Delta^{(l)}h_i^A$, $\Delta^{(l)}h_j^B$ in Eq. (13) represent the difference between feature descriptors of nodes in one graph and that of the closest neighbor nodes in the other graph, which can be described as

$$\begin{aligned} \Delta^{(l)}h_i &= {}^{(l)}h_i - a_{i\to j} \cdot {}^{(l)}h_j, \quad j \in V_B, \\ \Delta^{(l)}h_j &= {}^{(l)}h_j - a_{j\to i} \cdot {}^{(l)}h_i, \quad i \in V_A, \end{aligned} \tag{16}$$

where $a_{i\to j}$ and $a_{j\to i}$ are cross-attention weights, which are measured by the similarity between feature descriptors from different images $^{(l)}h_i$ and $^{(l)}h_j$. Here the similarity could be Euclidean or cosine similarity, and dot product similarity is adopted in this paper. The similarity matrix and the attention weights are expressed as

$$s = -\left|^{(l)}h_i - {}^{(l)}h_j\right|^2, \quad i \in V_A, j \in V_B, \tag{17}$$

$$\begin{aligned} a_{i\to j} &= \frac{\exp(s(^{(l)}h_i, {}^{(l)}h_j))}{\sum_j \exp(s(^{(l)}h_i, {}^{(l)}h_j))}, \\ a_{j\to i} &= \frac{\exp(s(^{(l)}h_i, {}^{(l)}h_j))}{\sum_i \exp(s(^{(l)}h_i, {}^{(l)}h_j))}. \end{aligned} \tag{18}$$

After Lth layers propagation of the graph node embedding network, the final feature descriptors f_j^B, f_j^B for star points from images A and B are linear projections, which can be expressed as

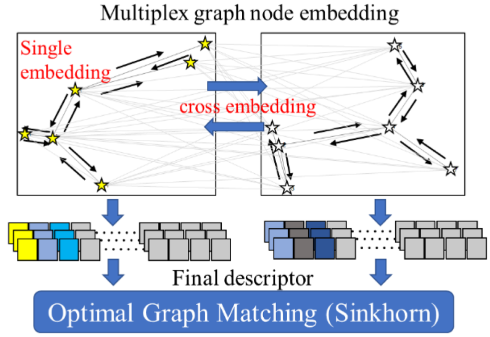

Fig. 8. Illustration of the multiplex graph node embedding. The single node embedding for intra-image is calculated by GAT through self-attention, and the cross-node embedding for inter-image is calculated through cross-attention. The final descriptors combine the multiplex node embeddings and do the linear projection.

Table 2. Algorithm 2: Multiplex Graph Node Embedding

Algorithm 2: Multiplex Graph Node Embedding
Input: lst layer graph data $G_A = \{^{(0)}h_i^A,\ E_{A(mst)}\},\ i \in V_A$, $G_B = \{^{(0)}h_j^B,\ E_{B(mst)}\},\ j \in V_B$
1. single graph node embedding $(^{(l)}h_i^A, ^{(l)}h_j^B),\ \forall i \in V_A, \forall j \in V_B$ by Eq. (14)
2. cross-graph attention $a_{i\to j}$ between two graphs by Eq. (18)
3. cross-graph aggregation $\Delta h_i^A, \Delta h_j^B$ by Eq. (16)
4. multiplex graph node features $^{(l+1)}h_i^A, ^{(l+1)}h_j^B\ \forall i \in V_A, \forall j \in V_B$ by Eq. (13)
Output: (l + 1)-th layer $G_A = \{^{(l+1)}h_i^A,\ E_{A(mst)}\},\ i \in V_A$, $G_B = \{^{(l+1)}h_j^B,\ E_{B(mst)}\},\ j \in V_B$

$$f_i^A = W \cdot {}^{(L)}h_i^A + b, \quad \forall i \in A,$$
$$f_j^B = W \cdot {}^{(L)}h_j^B + b, \quad \forall j \in B. \tag{19}$$

Algorithm 2 (Table 2) describes the multiplex graph node embedding.

4. Graph Optimal Matching

The final linear feature descriptors of star points convert the graph optimal matching problem from NP-hard to linear assignment [36]. The number of detected points in images A and B are M and N, respectively. And the score matrix $S \in R^{M\times N}$ with size of $M \times N$ between two different images based on the descriptors f_i^A, f_j^B can be expressed as

$$S_{i,j} = \langle f_i^A,\ f_i^B \rangle, \quad \forall (i,\ j) \in A \times B, \tag{20}$$

where $\langle , \rangle$ is the inner product, and $S \in R^{M\times N}$ describes the similarity of star points from different images. When the pair of stars i, j matched, $S_{i,j}$ should be the maximum value in both column and row. Therefore, the problem of finding the optimal matched points can be solved by finding an assignment matrix P that maximizes the value of $P_{i,j}$. The Sinkhorn algorithm is adopted by SuperGlue to solve the matrix and outputs the matched points, which is commonly used in the optimal transport problem [37].

3. EXPERIMENTS AND DISCUSSION

In this section, the simulation of star images for training and testing is presented first. Next, to illustrate the performance of the proposed MSG method, the matching precision and matching score are elaborated in detail. Finally, experiment results are analyzed, and the stitched star image is illustrated to prove the proposed SOCRI method.

The MSG networks are built on the Pytorch framework, the implementation tool is PyCharm Professional 2021, and the experiments are performed on a Windows 11 laptop (CPU is I5-10210U 1.60GHz, the memory is 8G) and a Linux server (GPU is 24G NVIDIA TESLA P40). During training, the dimension of pre-trained SuperPoint descriptors is 256, and the Adam optimizer is used for optimization; the learning rate is set to 1e-4. There are five layers of the multiplex graph node embedding (five layers are useful because the points in star images are not as much as in natural images), and each layer has four heads of attention. The Sinkhorn iteration is set to 100, and the matching threshold is set to 0.2, just the same setting as in SuperGlue. The average star image matching time of each 1024×1024 image is 101 ms, 9.91 FPS. In terms of storage, the size of the MSG model is 55.4 MB, which makes sure that the satellite would have enough computing resources for our algorithm [38].

A. Dataset Generation for Training and Testing

To validate the proposed MSG performance on star images, both the training and testing datasets are generated from the Tycho-2 star catalog based on the imaging principle under dynamic status for simulation experiments. In this work, the training dataset should be constructed to improve the learning ability of positions between star points. And the test dataset is constructed to objectively evaluate the performance of the proposed MSG. Table 3 shows the parameters setting for star images simulation. The parameters settings of the camera are the same to all simulated star images, such as the focal length, the FOV, and the pixel size of the detector. Therefore, stars in areas that change with the camera motion will be projected to the image plane. The right ascension and the declination of the optical axis direction of the camera in the camera body coordinate system are changing with the camera motions. Therefore, the right ascension and declination are set to different angles to generate simulated star images covering the whole space.

The main target of this work is to obtain stitched images containing as many stars and RSOs, which should avoid the length of star smearing being too long to affect star image matching and stitching. In this way, the angular velocity $\omega_z(\omega_o)$ is set to 2°/s, and $\omega_y(\omega_s)$ is set to 2°/s. In the training dataset, the right ascension and declination are set from 180° to 180°, respectively. For abundant scenes in the training dataset, the angle is set at 0.01° intervals to generate different star images from various views of the camera. So far, there are $(180 + 180)/0.01 + 1 = 36{,}001$ star images in the training dataset. As for the test dataset, the background noise (Gaussian noise is selected as background noise) and RSOs that have similar shape with smearing stars are added to the simulated images. And the right ascension and the declination are set at 1° intervals, respectively.

As mentioned in Section 2.A.2, smearing star images under dynamic states bring difficulty to feature extracting, which

Table 3. Parameters Setting for Star Images Simulation

Item	Parameter	Unit
Magnitude threshold of camera	8	Mv
Field of view	12×12	Deg(°)
Focal length	22	mm
Image dimensions	1024×1024	Pixel
Pixel size	0.012×0.012	Mm
Exposure time	50	ms
Radius of the point spread function	3	Pixel
Right ascension	−180 to 180	Deg(°)
Declination	−180 to 180	Deg(°)
Angular velocity $\omega_z(\omega_o)$	2	Deg/s(°/s)
Angular velocity $\omega_y(\omega_s)$	2	Deg/s(°/s)

will directly reduce the accuracy of the proposed MSG networks. There are some methods for image restoration that can make smearing image back to static point image [39]. For stable local features, we preprocess star images by removing the background noise and obvious smearing star points that generated from the camera motion [40]. Instead of labeling the input star image pairs by manual efforts to define true matching correspondences, we chose the self-supervised training method [41]. We perform random homographic warps on simulated star images to generate a pair of star images as the input of the proposed MSG network. The warped image is generated from the input image with random translation, rotation, and scaling operations. Since the transformation is random, the warped images are not repeated during training and testing, which increases the adaptability to different scenes. To generate pseudo-ground-truth correspondences, we first detect interest points using SuperPoint on the input image and the wrapped image, respectively. And the matching points are considered as pseudo-ground-truth correspondences if the corresponding epipolar error is smaller than matching threshold 5e-4.

B. Experiment Results

In the evaluation period, a set of star images in chronological order are given as the input, and the proposed MSG model then predicts the correspondence between two adjacent star images. To evaluate the matching performance of the MSG model from the predicted correspondence, matching precision (MP) and matching score (MS) are selected as evaluation matrices, which can be calculated separately as

$$\text{Matching Percision (MP)} = \frac{\text{correct matches}}{\text{predicted matches}},$$

$$\text{Matching Score (MS)} = \frac{\text{correct matches}}{\text{total star points}}, \tag{21}$$

where a match is considered as a truly correct match based on whether the epipolar distance is smaller than the predefined threshold 5e-4. Matches are predicted by the MSG model which contains correct and false matches, and the total star points are successfully detected by the SuperPoint model. MP and MS estimate the matching performance based on the number of correct matches, which are used commonly in image matching evaluation.

The purpose of the proposed MSG is to compute the optimal correspondences based on feature descriptors from two different star images. The MSG works in the middle of the image matching pipeline, which is after the feature description part and before the stitching part. Therefore, we test the proposed MSG algorithm in combination with SIFT and SP local features, and the nearest neighbors (NN) is used as the traditional matcher to compare with the deep learning method. The MSG is compared with different algorithms described as follows. The SIFT plus NN algorithm: this combination is a classic method for image matching, used to test the performance of the deep learning method over the traditional method. SIFT extracts key points by calculating the consistency of local orientation, and the local features are obtained by calculating the gradient histogram of the image aera that is around the key point. The SIFT plus MSG algorithm: this combination is used to evaluate how local features affect performance. The SP plus SG algorithm: this is the best combination in the original SuperGlue network [18]. Finally, we adopt the SP combined with the proposed MSG, because the SP model detects repeatable and stable key points and features which are efficient for matching.

Table 4. Matching Results of Proposed Algorithm Compared with Other Algorithms

Method	Matching Precision	Matching Score
SIFT + NN	0.6174	0.1018
SIFT + MSG	0.8193	0.1365
SP + SG	0.8964	0.1894
SP + MSG (ours)	0.9288	0.2073

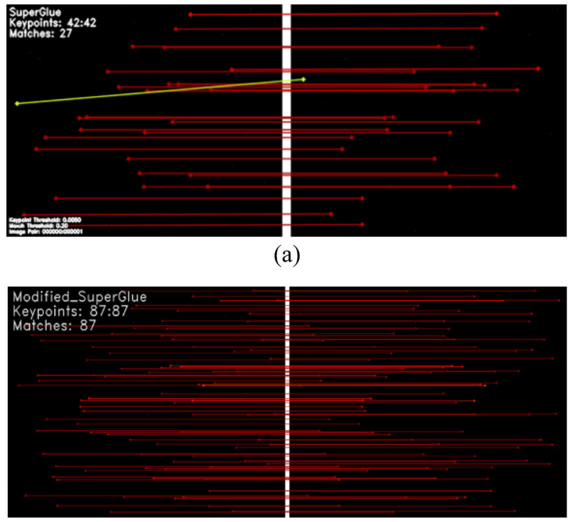

(a) (b)

Fig. 9. Matched star points visualization based on different methods, (a) SP + SG, (b) SP + MSG. The declination of two consecutive star images differs by 0.1°. The proposed method detects and matches points more correctly.

The comparative matching results are shown in Table 4. Obviously, the combination of the feature extraction SIFT with the traditional matcher NN method works terrible on star images. On the contrary, the proposed MSG method with SP significantly outperforms SIFT; the MP decreases from 0.9288 to 0.6174. It shows the power of the deep learning method based on the GNN for star images with fewer texture features over traditional methods. Specifically, the proposed MSG method with SP performs better than the SG with SP; the MP increases from 0.8964 to 0.9288, which proves that the topology position relationship between star points helps improve the matching precision. Figure 9 shows the matching of star images based on the proposed method and the SG method with SP. As can be seen, the proposed MSG network detects and matches star points more correctly.

The MSG network constructs stable star points features by calculating the typology graph which is based on the key points detected by the SuperPoint network. Therefore, the energy distribution of stars on the focal plane is important for the detection of the SuperPoint network, which determines the

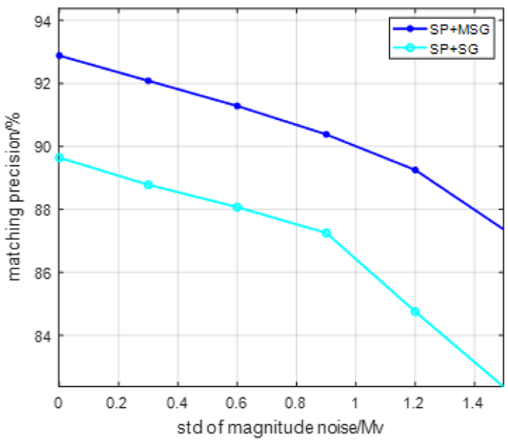

Fig. 10. Effects of magnitude noise on the matching precision.

Fig. 11. On-orbit real stellar image in [23].

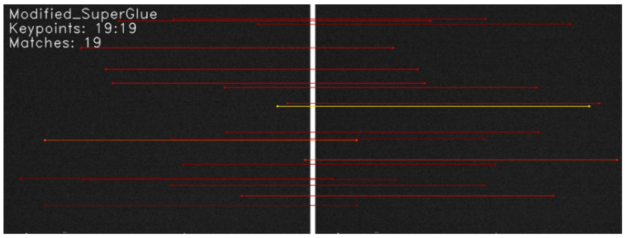

Fig. 12. Matched star points visualization on real stellar image for the MSG method.

Fig. 13. Multiframe star map stitching (the latitude of the simulated camera is from 45° to 75°).

matching precision. We performed the experiment of matching precision with different magnitudes; the magnitudes of stars are added with Gaussian random noise with the standard deviation ranging from 0 to 1.5 Mv. Figure 10 shows the influence of magnitude on the matching precision of the proposed method. The matching precision of the MSG method with SuperPoint dropped from 0.9288 to 0.8735 with the increase in magnitude noise. However, compared with the SuperGlue with SuperPoint methods, the MSG method is more robust to magnitude noise.

Obviously, it is hard to obtain real star images under the same dynamic conditions as our setup. Fortunately, the real on-orbit data in [22] is clearly enough for testing our method. The FOV and resolution of the star tracker are $19.7° \times 11.2°$ and 1920×1080 pixels, respectively. The magnitude threshold is set as 5 Mv, and the stellar image is shown in Fig. 11. As we can see, this is a static star image because the stars in the image are point-like shapes. To generate image pairs, we perform the same homographic translation on the on-orbit image as that used on the simulation star images. Figure 12 shows the matching of real star images based on the MSG with SuperPoint method.

C. Discussion

From matching experiment results in Table 4, the proposed MSG network mainly depends on the local feature descriptors obtained in the previous feature processing model. As we mentioned before, star images have less texture and gray information than natural images. The SIFT algorithm relies on the local image information to determine the orientation of detected points and realize the matching, which directly leads to the poor effect of matching points between star images with weak texture information. However, the bright star points are regularly distributed according to the topology position relations, which is more stable and effective than the texture information. The MSG method embeds the topology structure of star points into local feature descriptors to establish stable features due to the use of graph neural networks, so that the matching results are better than other baseline methods.

The results of the robustness experiment to magnitude noise show that the matching accuracy decreases as the magnitude noise increases. This is because the magnitude information affects the star energy and has an impact on the initial descriptors generated by the SuperPoint model. The modified SuperGlue network is more robust to magnitude noise over the original SuperGlue network. Also, the matching experiment on real star images shows that the proposed method performs well on static real on-orbit data. With the proposed method, we can train algorithms that suit various on-orbit images that even may not be available to users. We finally sequentially perform the stitching between two adjacent frames of a series of star images generated in a chronological order; the latitude range of the simulated camera is from 45° to 75°, and the stitching star image is shown in Fig. 13.

4. CONCLUSION

In this work, we proposed an optical circular rotation imaging method performed by a single space camera and a star image matching network MSG based on graph neural networks for obtaining a stitched large FOV star image. The SOCRI mode relies on only one inclined optical camera to capture star images by performing a rotational motion around the spin axis. Furthermore, the MSG network is proposed to precisely match star images that lack texture features and similar distribution of star points by graph node embedding of the star graph. The experimental results show that the network has a great improvement in matching precision and scores and is robust to magnitude noise. However, in the proposed matching method, we preprocess star images by removing background noise and recovering smearing star points, which is not a completely end-to-end matching network. Also, the scanning velocity of the SOCRI method is compromised to avoid the influence of long smearing on star map matching. In future work, we will continue to focus on directly matching smearing star images without any preprocessing and collecting real data under high dynamic conditions to validate our method. We hope that our method can be applied in practical space-based surveillance missions.

Funding. China Scholarship Council; National Natural Science Foundation of China (51874300, 52274160, 62005275, 62101071, 62171430).

Acknowledgment. The authors would like to thank all the reviewers for their valuable contributions to our work.

Disclosures. The authors declare no conflicts of interest.

Data availability. Data underlying the results presented in this paper are not publicly available at this time but may be obtained from the authors upon reasonable request.

REFERENCES

1. Y. Zhang, B. Li, H. Liu, and J. Sang, "An analysis of close approaches and probability of collisions between LEO resident space objects and mega constellations," Geo-spatial Inf. Sci. **25**, 104–120 (2022).
2. D. Cutajar, A. Magro, J. Borg, K. Z. Adami, G. Bianchi, A. Maccaferri, A. Mattana, G. Naldi, and G. Pupillo, "Track detection of high-velocity resident space objects in Low Earth Orbit," Adv. Space Res. **71**, 1670–1681 (2022).
3. S. Afshar, A. P. Nicholson, A. van Schaik, and G. Cohen, "Event-based object detection and tracking for space situational awareness," IEEE Sens. J. **20**, 15117–15132 (2020).
4. G. Soldi, D. Gaglione, N. Forti, A. Di Simone, F. C. Daffinà, G. Bottini, D. Quattrociocchi, L. M. Millefiori, P. Braca, and S. Carniel, "Space-based global maritime surveillance. Part I: Satellite technologies," IEEE Aerosp. Electron. Syst. Mag. **36**(9), 8–28 (2021).
5. H. Yunpeng, L. Kebo, L. Yan'gang, and C. Lei, "Review on strategies of space-based optical space situational awareness," J. Syst. Eng. Electron. **32**, 1152–1166 (2021).
6. F. Fang, T. Wang, Y. Fang, and G. Zhang, "Fast color blending for seamless image stitching," IEEE Geosci. Remote Sens. Lett. **16**, 1115–1119 (2019).
7. S. El Fellah, M. Rziza, and M. El Haziti, "An efficient approach for filling gaps in Landsat 7 satellite images," IEEE Geosci. Remote Sens. Lett. **14**, 62–66 (2016).
8. N. N. Das, D. Entekhabi, R. S. Dunbar, M. J. Chaubell, A. Colliander, S. Yueh, T. Jagdhuber, F. Chen, W. Crow, and P. E. O'Neill, "The SMAP and Copernicus Sentinel 1A/B microwave active-passive high resolution surface soil moisture product," Remote Sens. Environ. **233**, 111380 (2019).
9. J. Du, X. Yang, M. Zhou, Z. Tu, S. Wang, X. Tang, L. Cao, and X. Zhao, "Fast multi-spectral fusion and high-precision inter-detector image stitching of agile satellites based on velocity vector field," IEEE Sens. J. **22**, 22134–22147 (2022).
10. T. Prusti, J. De Bruijne, A. G. Brown, A. Vallenari, C. Babusiaux, C. Bailer-Jones, U. Bastian, M. Biermann, D. W. Evans, and L. Eyer, "The GAIA mission," Astron. Astrophys. **595**, A1 (2016).
11. F. Wang, R. Xi, C. Yue, H. Li, and X. Cao, "Conceptual rotational mode design for optical conical scanning imaging small satellites," Sci. China Technol. Sci. **63**, 1383–1395 (2020).
12. D. Liu, B. Chen, T.-J. Chin, and M. G. Rutten, "Topological sweep for multi-target detection of geostationary space objects," IEEE Trans. Signal Process. **68**, 5166–5177 (2020).
13. Y. Ding, Z. Zhang, X. Zhao, D. Hong, W. Cai, N. Yang, and B. Wang, "Multi-scale receptive fields: graph attention neural network for hyperspectral image classification," Expert Syst. Appl. **223**, 119858 (2023).
14. X. Yuan, X. Yuan, J. Chen, and X. Wang, "Large aerial image tie point matching in real and difficult survey areas via deep learning method," Remote Sens. **14**, 3907 (2022).
15. Y. Ding, X. Zhao, Z. Zhang, W. Cai, N. Yang, and Y. Zhan, "Semi-supervised locality preserving dense graph neural network with ARMA filters and context-aware learning for hyperspectral image classification," IEEE Trans. Geosci. Remote Sens. **60**, 5511812 (2021).
16. Z. Zhang, Y. Ding, X. Zhao, L. Siye, N. Yang, Y. Cai, and Y. Zhan, "Multireceptive field: An adaptive path aggregation graph neural framework for hyperspectral image classification," Expert Syst. Appl. **217**, 119508 (2023).
17. Y. Cai, L. Li, D. Wang, X. Li, and X. Liu, "HTMatch: an efficient hybrid transformer based graph neural network for local feature matching," Signal Process. **204**, 108859 (2022).
18. P.-E. Sarlin, D. DeTone, T. Malisiewicz, and A. Rabinovich, "Superglue: Learning feature matching with graph neural networks," in *Proceedings of the IEEE/CVF Conference on Computer Vision and Pattern Recognition* (2020), pp. 4938–4947.
19. J. Ma, X. Jiang, A. Fan, J. Jiang, and J. Yan, "Image matching from handcrafted to deep features: A survey," Int. J. Comput. Vis. **129**, 23–79 (2021).
20. S. Qiu, D. Zhou, and Y. Du, "The image stitching algorithm based on aggregated star groups," Signal Image Video Process. **13**, 227–235 (2019).
21. Y. Du, D. Wen, G. Liu, S. Qiu, and N. Li, "A characteristic extraction algorithm based on blocking star images," Int. J. Pattern Recognit. Artif. Intell. **33**, 1954028 (2019).
22. Z. You, J. Li, H. Zhang, B. Yang, and X. Le, "An accurate star identification approach based on spectral graph matching for attitude measurement of spacecraft," Complex Intell. Syst. **8**, 1639–1652 (2022).
23. P. Veličković, G. Cucurull, A. Casanova, A. Romero, P. Lio, and Y. Bengio, "Graph attention networks," arXiv, arXiv:1710.10903 (2017).
24. T. N. Kipf and M. Welling, "Semi-supervised classification with graph convolutional networks," arXiv, arXiv:1609.02907 (2016).
25. B. R. Hancock, R. C. Stirbl, T. J. Cunningham, B. Pain, C. J. Wrigley, and P. G. Ringold, "CMOS active pixel sensor specific performance effects on star tracker/imager position accuracy," Proc. SPIE **4284**, 43–53 (2001).
26. Y. Li, X. Wei, J. Li, and G. Wang, "Error correction of rolling shutter effect for star sensor based on angular distance invariance using single frame star image," IEEE Trans. Instrum. Meas. **71**, 7003213 (2022).
27. H. Yuan, K. Lu, and Q. Liu, "Motion modeling and blurred image simulation of the star tracker used for deep-space missions," J. Opt. Soc. Am. B **39**, 2934–2943 (2022).
28. J. Han, X. Yang, T. Xu, Z. Fu, L. Chang, C. Yang, and G. Jin, "An end-to-end identification algorithm for smearing star image," Remote Sens. **13**, 4541 (2021).
29. J. Zhou, G. Cui, S. Hu, Z. Zhang, C. Yang, Z. Liu, L. Wang, C. Li, and M. Sun, "Graph neural networks: A review of methods and applications," AI Open **1**, 57–81 (2020).
30. D. DeTone, T. Malisiewicz, and A. Rabinovich, "Superpoint: Self-supervised interest point detection and description," in *Proceedings of the IEEE Conference on Computer Vision and Pattern Recognition Workshops* (2018), pp. 224–236.
31. O. Viniavskyi, M. Dobko, D. Mishkin, and O. Dobosevych, "OpenGlue: Open source graph neural net based pipeline for image matching," arXiv, arXiv:2204.08870 (2022).
32. V. Schiattarella, D. Spiller, and F. Curti, "Star identification robust to angular rates and false objects with rolling shutter compensation," Acta Astronaut. **166**, 243–259 (2020).
33. M. Chakraborty, S. Chowdhury, J. Chakraborty, R. Mehera, and R. K. Pal, "Algorithms for generating all possible spanning trees of a simple undirected connected graph: an extensive review," Complex Intell. Syst. **5**, 265–281 (2019).
34. Y. Li, C. Gu, T. Dullien, O. Vinyals, and P. Kohli, "Graph matching networks for learning the similarity of graph structured objects,"

in *International Conference on Machine Learning (PMLR)* (2019), pp. 3835–3845.

35. R. Wang, J. Yan, and X. Yang, “Learning combinatorial embedding networks for deep graph matching,” in *Proceedings of the IEEE/CVF International Conference on Computer Vision* (2019), pp. 3056–3065.
36. J. Hartmanis, “Computers and intractability: a guide to the theory of np-completeness (Michael R. Garey and David S. Johnson),” SIAM Rev. **24**, 90 (1982).
37. K. Pham, K. Le, N. Ho, T. Pham, and H. Bui, “On unbalanced optimal transport: An analysis of Sinkhorn algorithm,” in *International Conference on Machine Learning (PMLR)* (2020), pp. 7673–7682.
38. Z. Fu, X. Yang, M. Wu, A. Yan, J. Du, S. Gao, and X. Tang, “Analysis and correction of the rolling shutter effect for a star tracker based on particle swarm optimization,” Remote Sens. **14**, 5772 (2022).
39. J. Jiang, J. Huang, and G. Zhang, “An accelerated motion blurred star restoration based on single image,” IEEE Sens. J. **17**, 1306–1315 (2016).
40. M. Wu, L. Chang, X. Yang, L. Jiang, M. Zhou, S. Gao, and Q. Pan, “Infrared small target detection by modified density peaks searching and local gray difference,” in *Photonics* (Multidisciplinary Digital Publishing Institute, 2022), p. 311.
41. Y. Ding, Z. Zhang, X. Zhao, W. Cai, N. Yang, H. Hu, X. Huang, Y. Cao, and W. Cai, “Unsupervised self-correlated learning smoothy enhanced locality preserving graph convolution embedding clustering for hyperspectral images,” IEEE Trans. Geosci. Remote Sens. **60**, 5536716 (2022).